Ocean Engineering 309 (2024) 118468

Contents lists available at ScienceDirect

Ocean Engineering

journal homepage: www.elsevier.com/locate/oceaneng

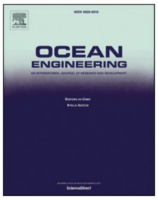

Research paper

Experimental and data-driven prediction for the impact of free/bond lengths of element specimen on interface characterization of ground anchors

Genbao Zhang [a,b], Changjie Xu [b], Yufei Wang [b,c], Junbo Sun [b,d,*], Haibin Ding [b], Shimin Zhu [e], Zefeng Zou [f], Hisham Al azzani [d], Zhiping Li [b], Danqi Li [g], Xiangyu Wang [b]

[a] College of Civil Engineering, Hunan City University, Yiyang, Hunan, 413000, China
[b] School of Civil Engineering and Architecture, East China Jiaotong University, Nanchang, 330013, Jiangxi, China
[c] School of Design and Built Environment, Curtin University, Perth, WA 6102, Australia
[d] Institute for Smart City of Chongqing University in Liyang, Chongqing University, Jiangsu, 213300, China
[e] School of Civil Engineering, Ludong University, Yantai, 264025, China
[f] School of Information Engineering, East China Jiaotong University, Jiangxi, 330013, China
[g] Faculty of Science and Engineering, WASM: Minerals, Energy and Chemical Engineering, Curtin University, China

ARTICLE INFO

Keywords:
Ground anchor
Element specimen
Free/bond lengths
Interface shear strength
Pullout test
Machine learning

ABSTRACT

The performance of ground anchor often employed in retaining the stability of onshore structures depends largely on its interface shear behavior. Interface characterization using pullout tests on element specimens of ground anchor is a versatile approach for determining its interface shear behavior. This research combines laboratory experiments and data-driven modeling to investigate the effect of free/bond lengths as a critical configuration condition of element specimen on the interface characterization results of ground anchors. Machine Learning models such as back propagation neural network (BPNN), random forest (RF), and support vector regression (SVR) were employed. Moreover, the particle swarm optimization (PSO) algorithm was used to improve the process. The results indicate that variations in free/bond lengths have a negligible effect on the trends of interface bond curves when bond lengths reach 90–100 mm. Moreover, when the bond and free lengths are set to 80 mm and 20 mm, respectively, the configuration conditions of the element specimen have a limited effect on the average interface shear strength. The PSO-BPNN model provided the most accurate predictions, which closely followed the experimental results compared to RF and SVR models. Compared to the other models, it reached a greater correlation coefficient (0.9975) and a lower root-mean-square error (14.89 kPa). Moreover, Partial dependence plot (PDP) is introduced to visualize the established machine learning model.

1. Introduction

Ground anchors have been extensively adopted in ocean engineering to ensure the in-service performance of onshore and offshore structures by retaining their stability when subjected to the wind-wave induced shaking and floating (Fontana Casey et al., 2019). Many researched have investigated the anchor theories and proposed various anchor systems such as a shared multiline anchor system (Fontana Casey et al., 2019), Hall anchor (Zhang et al., 2023), anchor plate (Hu et al., 2023), etc. The bearing capacity of an ground anchor is dependent on the shear characteristics of its anchoring interface, which can only be accurately calculated by utilizing an anchorage interface bond-slip models (Ren et al., 2010; Zou and Zhang, 2019; Sun et al., 2021a). Generally, there are two main approaches for calculating anchorage interfacial characteristics. The first is the semi-empirical field approach, which utilizes in-situ pullout test data of engineering anchors for back analysis (Cheng et al., 2016; Cao et al., 2023a; Cao et al., 2023b). The second approach measures anchorage interface behavior by performing pullout tests on actual element anchors specimens (Chen et al., 2019; Zhang et al., 2020a; Chen et al., 2018; Chen et al., 2020). In contrast to the

---

* Corresponding author. School of Civil Engineering and Architecture, East China Jiaotong University, Nanchang, 330013, Jiangxi, China.

E-mail addresses: genbao@hncu.edu.cn (G. Zhang), xucj@zju.edu.cn (C. Xu), wangyf0113_suz@163.com (Y. Wang), tunneltc@gmail.com (J. Sun), hbding@ecjtu.edu.cn (H. Ding), smzhu@ldu.edu.cn (S. Zhu), zoutze@outlook.com (Z. Zou), hisham.alazzani@gmail.com (H. Al azzani), lizhiping@ecjtu.edu.cn (Z. Li), Danqi.Li@curtin.edu.au (D. Li), Xiangyu.Wang@curtin.edu.au (X. Wang).

https://doi.org/10.1016/j.oceaneng.2024.118468
Received 10 December 2023; Received in revised form 16 March 2024; Accepted 10 June 2024

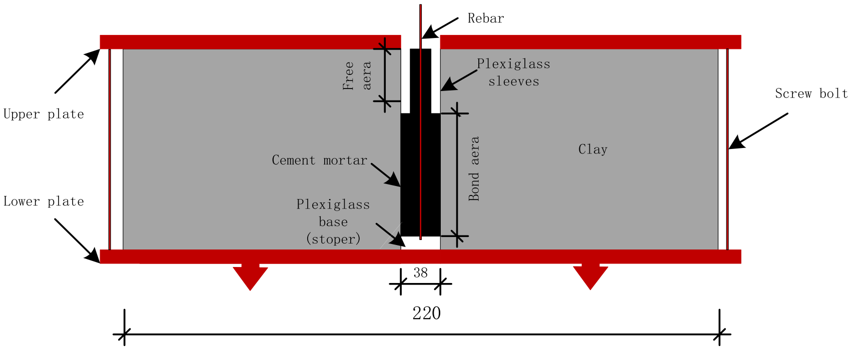

Fig. 1. Schematic of the element anchor specimens.

experimental approach, in which specific conditions and experiment costs can restrict, the laboratory method allows the physical simulation of anchorage interfaces under actual situations by designing varying testing configurations.

For various anchorage interfaces, several researchers have developed theoretical (Zhang et al., 2022a) or data-driven (Zhang et al., 2022b; Ren et al., 2022; Zhang et al., 2022c) bond-slip models, as well as time-dependent rheological interface models (Zhu et al., 2022; Chen et al., 2021; Chen et al., 2022a). These models were built based on considerable data analysis and have proven beneficial for accurately describing the interfacial characteristics of anchorages. Hence, there is a growing demand for laboratory anchorage interface characterization that simulates field conditions accurately.

In the experimental evaluation of grouted anchors and rock bolts, the use of element specimens to characterize anchorage interfaces (Chen et al., 2019; Bjarte et al., 2023) is a common approach. By applying pullout loading to short anchors and monitoring the load and displacement data at the anchor head, an interface bond-slip model can be developed based on the stress-strain homogenization assumption (Zhang et al., 2020a; Chen et al., 2018; Chen et al., 2020). Anchorage interface characterization relies significantly on the characteristics of the anchor specimen. Nevertheless, the effect of bond-length and boundary conditions on element anchor specimens has not been thoroughly explored. Furthermore, experimental evaluation of interface bond strength is both costly and time-consuming due to the complex equipment and large sample sizes required for experimental configurations (José Antonio et al., 2019; Aiqing et al., 2023; Zhang et al., 2024a). In addition, traditional data analysis methods have limitations in terms of error control and obtaining optimal balance proportions under multivariable conditions. While multiple linear regression (MLR) and logistic regression (LR) are commonly used, issues related to the burden of dimensionality and susceptibility to co-linearity can result in unreliable simulations (Fernández-Martínez et al., 2020; Yan et al., 2023; HUANG et al., 2022). Consequently, there is a growing need for improved models to investigate the effect of bond length on the interface bond strength.

In building materials and construction, artificial intelligence (AI) approaches are frequently used to overcome the gap between inputs (datasets) and outputs (results) (Sun et al., 2021b; Wanhui et al., 2022; Sun et al., 2022a). For example, For an Ensemble Learning Approach, the random forest (RF) leads the prediction of concrete conductivity (Sun et al., 2021b; Sun et al., 2021c), while the artificial neural network (ANN) excels at predicting the strength of concrete (Sun et al., 2021d; Sun et al., 2022b; Sun et al., 2022c). The excellent ability of the support vector regression (SVR) to adapt and compute allows it to be prominent in the area of data mining (Sun et al., 2021c; Yao et al., 2023; Zhang et al., 2024b). Using AI to process datasets in complex experimental studies reduces costs as well as time (Sun et al., 2019a). Back propagation neural network (BPNN) is the most versatile and prevalent approach. Engineers only have to modify the neural network configuration, making it simple and quick to program (Vinay et al., 2015; Wang et al., 2022). BPNN parallel processing on a large scale offers an infrastructure for the constant and efficient evaluation of any object. Therefore, BPNN has been extensively used for predicting and evaluating the mechanical properties of different materials.

Even though BPNN is widely used, its development involves numerous repetitive training procedures. The volume of hidden layers and the number of neurons in each layer, are two key hyperparameters that directly influence the performance of BPNN (Sun et al., 2019a; Yang et al., 2023). Creating the appropriate BPNN framework with the right hyperparameters takes considerable effort and time, which slows down the process (Sun et al., 2020). To address this, this study utilized the particle swarm optimization (PSO) algorithm to modify the BPNN framework. PSO is a straightforward heuristic approach and stochastic method that is well-balanced and adaptable, making it suitable for improving global and local searches (Abido, 2002; Chen et al., 2022b; Yuanbo et al., 2021).Compared to other optimization methods, it is more computationally efficient, requires less memory, and is simpler to execute (Medvedeva et al., 2020; Zhang et al., 2020b). Combining these two methods, the volume of hidden layers, the number of neurons within, and the connection weights were modified to save additional effort and time. Due to the PSO algorithm's exceptional robustness, rapid convergence, and gratifying distributed capability, the enhanced framework predicted bond strength more accurately.

The main objective of this study is to investigate the effect of free/bond length configuration conditions on the interface bond strength. To achieve this objective, 48-element anchor specimens with different bond/free length ratios were fabricated and tested. The obtained test results were performed as the training data for the PSO-BPNN model. To investigate the error in both testing as well as training datasets, the optimal BPNN was implemented in both datasets. In addition, computed correlation coefficients were used to assess the relationship between the predicted and calculated outcomes generated by this model. Finally, a sensitivity analysis was conducted to determine the priority of the input variables.

2. Experimental test

2.1. Test program

As described in previous literature (Cheng-Yu et al., 2016), the characterization of anchor interface frictional behavior necessitated the use of a specifically made system during specimen preparation and pullout testing. The water content and dry density of the adjacent soil were maintained throughout the testing procedure. The design of the element anchor specimens was varied by changing the ratio of the bond/free length, with the free section of the anchorage being developed to maintain a constant interface contact area and prevent variations in the anchor element size. The free section of the specimen is prepared by placing a plexiglass tube to separate the cement mortar with the soils when the anchor hole is grouted, and removing the plexiglass

Table 1
Combinations of element anchor specimens.

Bond length (mm)	Free length (mm)					
	20	30	40	50	60	70
30	30/20	30/30	30/40	30/50	30/60	30/70
40	40/20	40/30	40/40	40/50	40/60	40/70
50	50/20	50/30	50/40	50/50	50/60	50/70
60	60/20	60/30	60/40	60/50	60/60	60/70
70	70/20	70/30	70/40	70/50	70/60	70/70
80	80/20	80/30	80/40	80/50	80/60	80/70
90	90/20	90/30	90/40	90/50	90/60	90/70
100	100/20	100/30	100/40	100/50	100/60	100/70

Table 2
Properties of the used materials.

Properties	Values/Description
Clay sample	
Specific gravity	2.69
Plastic limit (%)	20.9
Liquid limit (%)	36.8
Maximum dry density (g/cm3)	1.92
Optimal moisture content (%)	17.2
Nonuniformity coefficient C_u	3.75
Coefficient of curvature C_c	0.42
Cement mortar sample	
Sand type	Medium sand
Cement type	P.O 42.5
Water/cement ratio (%)	45
Grouting type	Gravity
Reinforcement sample	
Rebar type	HRB400
Diameter (mm)	8
Tensile strength (MPa)	540
Elastic modulus (GPa)	231.4
Yield strength (MPa)	400

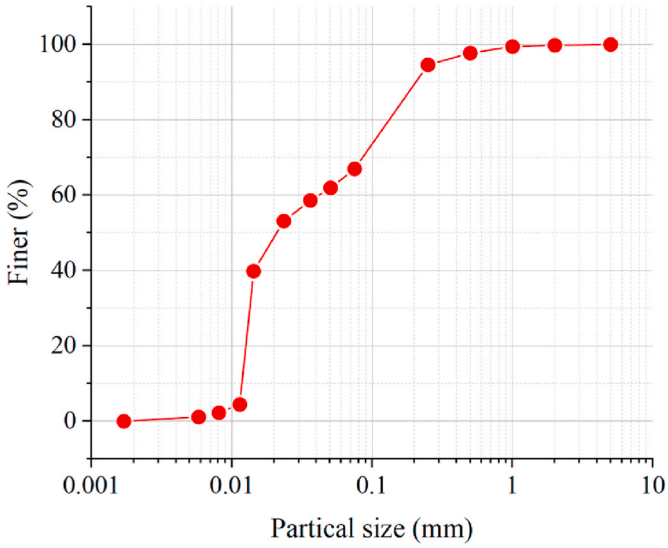

Fig. 2. Particle gradation curve of the clay sample used in the test.

tube when the grouting gets hardened.

The specimens were manufactured with a 38 mm diameter anchor opening and 30–100 mm bond lengths. To accommodate the maximum allowable pullout displacement of the loading device which is 20 mm, the unrestrained length was varied between 20 and 70 mm. In addition, a 10-mm thickness plexiglass stopper was placed at the bottom of the anchor opening to ensure rebar alignment and prevent the cement mortar from overflowing, resulting in an overall height of 60–180 mm for each specimen. Fig. 1 depicts the design of element anchor specimens with varying bond/free length ratios. Table 1 lists the various bond/free length ratios. The specimens were split into eight groups based on bond length, with six different free lengths in each group.

2.2. Material properties

The unit anchor sample in this test requires clay, steel bars, and a grouting mortar. The natural clay used was obtained from the Xiangjiang River in the City of Changsha, China, and was processed by removing impurities and passing it through a 5 mm sieve. The physical and mechanical properties of the clay were tested in the laboratory, and the relevant parameters are listed in Table 2, while the gradation curve is illustrated in Fig. 2. The grouting mortar material utilized in this test is cement mortar with a water-cement ratio of 0.45. The reinforcement body consists of HRB400 deformed steel bars, with corresponding material parameters also listed in Table 2.

3. Machine learning models

3.1. Back propagation neural network (BPNN)

The interface bond strength affected by input interactions was modeled using artificial neural networks (ANN). Typically, neural network layers comprise neurons with multiple inputs and a single output, which form functional input-output connections. Each neuron serves as a calculation cell within the equation.

$$y = \max\left(0, \sum_i w_i x_i + b\right) \tag{1}$$

where y and x_i is the values of output and input in each neuron; w_i is the connection weight; b is the bias value.

Eqs. (2) and (3) below are used to build a mapping between inputs and outputs:

$$h_i = \max(0, W_i \cdot h_{i-1} + b_i)\text{for } 1 \le i \le L, \text{and } h_0 = x \tag{2}$$

$$y = \max(0, V \cdot h_L) \tag{3}$$

where L is the numbers of the layer; matrices $W_1, \ldots W_L, V$, and vectors b_1, $\ldots b_L$ are the model parameters obtained from the dataset.

The neural network architecture includes hidden, input, and output layers. In this study, the volume and number of neurons in the hidden layer were considered as key factors for accurate predictions, and selecting appropriate hyperparameters is critical to the configuration of the ANN. To determine optimal hyperparameters, the particle swarm optimization (PSO) algorithm was utilized. The second layer receives the output from the first layer after model configuration. The feedforward network architecture, shown in Fig. 3(a), was employed as it is known for its high performance. The output layer's performance was further enhanced by using the following activation function:

$$f(x) = \frac{2}{1 + exp(-x)} - 1 \tag{4}$$

In Fig. 3(b), the back-propagation (BP) algorithm is used to train an ANN for optimization. During each iteration, the network calculates the difference between the anticipated and computed output values and transmits it backward through multiple layers. The mean square error (MSE) within the projected and observed outputs is reduced by iterating and modifying weights. The weight is immediately adjusted based on the error gradient using the steepest gradient descent method, as shown in Eq. (5) (Shi et al., 2020):

$$\Delta w_n = \alpha \Delta w_{n-1} - \eta \frac{\partial E}{\partial w} \tag{5}$$

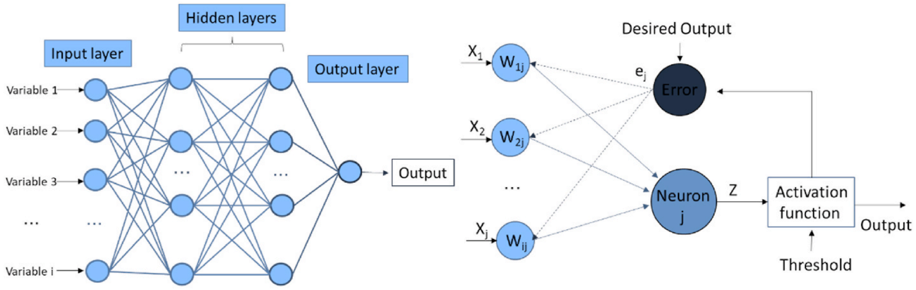

(a) ANN structure (b) BP procedure

Fig. 3. Architecture of neural networks (WANHUI et al., 2022).

Table 3
Statistics of the dataset.

Input variables and output	Minimum	Maximum	Mean	Std Dev.
Bond length (mm)	30	100	70	23.1
Free length (mm)	20	70	40	17.2
Displacement (mm)	0	24.8	8.5	5.27
Force (N)	0	666.24	479.76	146.78

when w is the weight between two neurons, Δw_n and Δw_{n-1} are the weight variation when repeated n and $n-1$ times, α and η and are the momentum factor and learning rate.

Following training, the network can acquire additional input modes to provide adequate output and mapping after determining the final connection weights. PSO will adjust BPNN's hidden layers, neurons per layer, bias values, and connection weights (Wanhui et al., 2022).

In this study, the variables are bond length, free length, and displacement, and the output is the force.

The dataset comprises 8630 data derived from the experimental results and the descriptive statistics can be viewed in Table 3. The minimum, maximum, mean value, and standard deviation indicate the smallest measurement, largest measurement, central tendency, and the amount of variation recorded in this study, respectively. These statistics offer insights into the measurements' distribution and variability, which are critical for quality control, design specifications, and further statistical analysis. The ML and optimization experiments are both implemented through Matlab R2020a.

3.2. Random frost (RF)

RF generates multiple decision trees (RTs) using "bagging" and "voting" to generate the final outcome (Schapire Denison et al., 2003). Fig. 4 shows the RF algorithm, where during each RT's training phase, n random variables are chosen without replacement from the training set. This approach is called "bootstrap," and the random variables are expressed by R_n in Eq. (6). After the training phase, the input data R_n is distributed from the root node to the leaf node, and the prediction function ($\hat{a}$ (X, R_n^{θ})) is produced. The RF consists of k decorrelated RTs to develop k forecast functions ($\hat{a}$ $(X, R_n^{\theta k})$). Eq. (7) shows that the final forecast Y is derived by averaging the k outputs $\{Y_1, Y_2, \dots Y_k\}$ (Breiman, 1996).

$$R_n = \{(X_1, Y_1), (X_2, Y_2), \text{‘}.(X_n, Y_n)\} \tag{6}$$

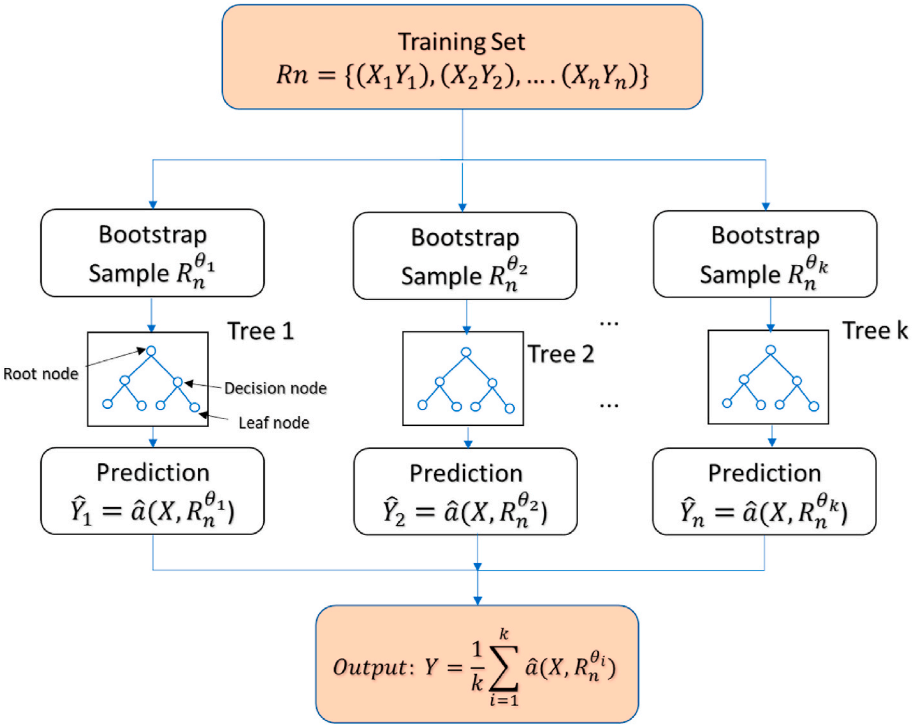

Fig. 4. Construction of the RF model (SUN et al., 2021b).

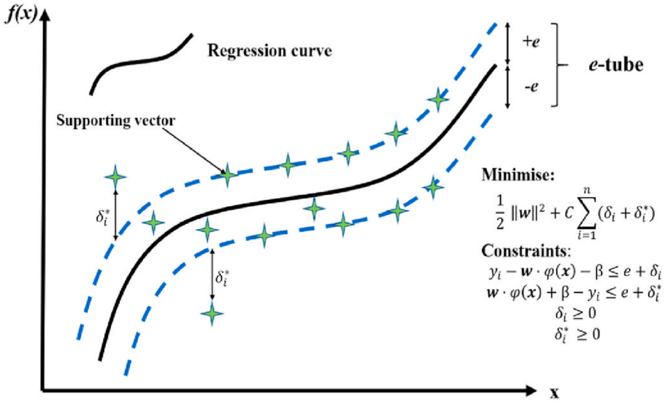

Fig. 5. A support vector regression machine (LAHIRI et al., 2008).

$$\frac{1}{k}\sum_{i=1}^{k} \hat{a}\left(X, R_n^{\theta i}\right) \tag{7}$$

3.3. *Support vector regression (SVR)*

SVR is a widely used model developed by Vapnik in 1995 that employs a kernel function which projects original data from its space to high dimensional space, thereby facilitating solutions of nonlinear queries (Burges, 1998). The data being processed is given as a set of (X_i, Y_i) pairs, with X_i being a one dimensional vector and Y_i being a scalar regression value. For an n-point training dataset, these pairs are represented as (X_n, Y_n). As shown in Eq. (8), the regression function can be defined as a linear equation:

$$f(x) = w \bullet \varphi(x) + \beta \tag{8}$$

where w represents the weight vector, β denotes the bias, and $\varphi(x)$ is the mapping function.

Eq. (9) is used to compute the magnitude of deviation between predicted and actual values.

$$\mathscr{L}(x, y, f) = |y_i - f(x_i)|_e = \begin{cases} 0, |y_i - f(x_i)| < e \\ |y_i - f(x_i)| - e_i, |y_i - f(x_i)| \ge e \end{cases} \tag{9}$$

Where e is the highest toleration error.

Given the lowest possible structural risk, the following definition of the problem is as follows:

$$\mathscr{R}(w) = \frac{1}{2}\|w\|^2 + \sum_{i=1}^{n}\mathscr{L}(x, y, f) \tag{10}$$

The following procedure can be used to convert the previous equation to a convex optimized function:

$$min_{w,e,\delta,\delta^*}\ \mathscr{R}(w) = \frac{1}{2}\|w\|^2 + C\sum_{i=1}^{n}(\delta_i + \delta_i^*)$$

$$s.t \begin{cases} y_i - w \cdot \varphi(x) - \beta \le e + \delta_i \\ w \cdot \varphi(x) + \beta - y_i \le e + \delta_i^* \\ \delta_i \ge 0 \\ \delta_i^* \ge 0 \end{cases} \tag{11}$$

where δ_i and δ_i^* employed to enhance the tolerance for biased data, and C represents the penalty coefficient.

The penalty coefficient C is determined based on a few distinctions between the regression lines and e-tube samples. The schematic illustration of SVR is depicted in Fig. 5. By introducing positive multipliers of Lagrange (α_i, α_i^*, u_i, u_i^*), Eq. (12) represents a dual-issue as follows:

$$L(w, \beta, \delta, a, u) = \frac{1}{2}\|w\|^2 + C\sum_{i=1}^{n}(\delta_i + \delta_i^*)$$

$$-\sum_{i=1}^{n} a_i(e + \delta_i - y_i + w \cdot \varphi(x_i) + \beta)$$

$$-\sum_{i=1}^{n} a_i^*(e + \delta_i + y_i - w \cdot \varphi(x_i) - \beta)$$

$$-\sum_{i=1}^{n}(u_i\delta_i + u_i^*\delta_i^*) \tag{12}$$

Eq. (13) must conclude the Kush-Kuhn-Tuck (KKT) rule for the first and second points, when the imperative condition is totally opposite and the target equation is distinct (Boyd et al., 2004). In Eq. (14), this rule dictates that the outcomes of dual variables and corresponding limits are *0*. In addition, the weight factor w takes the following form $\sum_{i=1}^{n}(a_i - a_i^*)\varphi(\boldsymbol{x}_i)$.

$$\begin{cases} \dfrac{\partial L}{\partial w} = w - \sum_{i=1}^{n}(a_i - a_i^*)\ \varphi(x_i) = 0 \\ \dfrac{\partial L}{\partial \beta} = \sum_{i=1}^{n}(a_i - a_i^*) = 0 \\ C - a_i - u_i = 0 \\ C - a_i^* - u_i^* = 0 \end{cases} \tag{13}$$

$$\begin{aligned} a_i(e + \delta_i - y_i + w \cdot \varphi(x_i) + \beta) = 0 \\ a_i^*(e + \delta_i + y_i - w \cdot \varphi(x_i) - \beta) = 0 \\ (C - a_i)\delta_i = 0 \\ (C - a_i^*)\delta_i^* = 0 \end{aligned} \tag{14}$$

Following the solution of the preceding equations, the Lagrange dual problem can be obtained in the following manner:

$$max_i\left(-\frac{1}{2}\sum_{i=1}^{n}\sum_{j=1}^{n}(a_i - a_i^*)\left(a_j - a_j^*\right)x_j^T x_j - e \right.$$

$$\left. \times \sum_{i=1}^{n}(a_i - a_i^*) + \sum_{i=1}^{n} y_i(a_i - a_i^*)\right)$$

$$s.t \begin{cases} \sum_{i=1}^{n}(a_i - a_i^*) = 0 \\ a_i, a_i^* \in [54] \end{cases} \tag{15}$$

Eq. (16) depicts the final regression function, as follows:

$$f(x) = \sum_{i=1}^{n}(a_i - a_i^*)\varphi(x_i)x + \beta \tag{16}$$

3.4. *Baseline models*

The PSO-BPNN models were compared to LR and MLR to verify the precision of their predictions. Eq. (17) shows the LR model with several predictive parameters.

$$ln\frac{p}{1 - p} = b_0 + \sum_{k=1}^{n} b_k x_k \tag{17}$$

where x_k and p are independent and dependent variate, respectively, b_0 and b_k are constant coefficients. Eq. (18) gives the relationship between the output variable Y and multiple predictive variables x_n in the MLR model (Sun et al., 2019b).

$$Y = \beta_0 + \beta_1 x_1 + \beta_1 x_2 + \ldots + \beta_n x_n \tag{18}$$

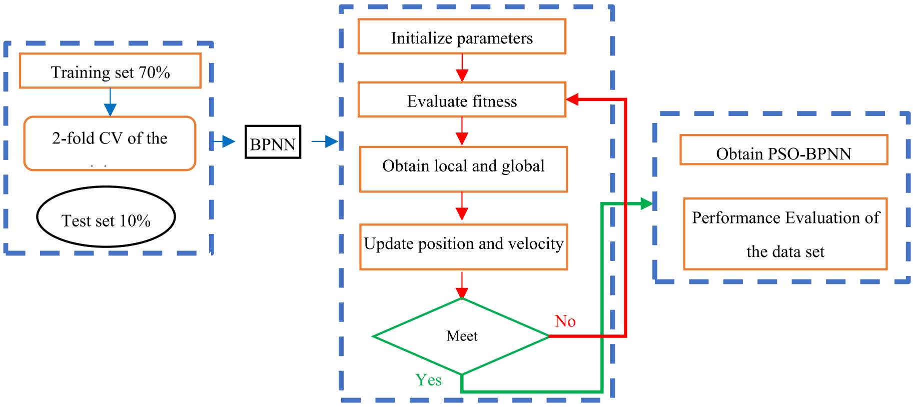

Fig. 6. BPNN model training by PSO.

where $\beta_1, \ldots, \beta_n$ are the regression coefficients.

3.5. Particle swarm optimization (PSO)

The PSO algorithm adjusts hyperparameters for the BPNN, SVR, and RF models by searching within a defined range of possible solutions. The PSO-BPNN algorithm uses particles to represent the two hyperparameters, specifically the number of hidden layers and neurons in each layer. The PSO algorithm sets the number of hidden layers between 1 and 3, and adjusts the number of neurons in each layer over 50 iterations to minimize the root-mean-square error (RMSE) over the validation dataset. The neuron range is empirically defined as 1–20, with a starting point of 10. Particle orientation is updated based on past and current best positions of the swarm, as shown below:

$$v_{id}^{t+1} = w \times v_{id}^{t} + C_1 \times r_{1i} \times \left(pbest_{id} - x_{id}^{t}\right) + C_2 \times r_{2i} \times \left(gbest_{id} - x_{id}^{t}\right) \tag{19}$$

$$x_{id}^{t+1} = x_{id}^{t} + v_{id}^{t+1} \tag{20}$$

where d is the dimension of the searching scope; v_{id}^{t} and v_{id}^{t+1} are the velocities of particle i at t and $t+1$ times; x_{id}^{t} and x_{id}^{t+1} are the coordinates of particle i at t and $t+1$ times; $pbest_{id}$ and $gbest_{id}$ are the best-given location of the particle and the whole swarm, respectively; w is the original weight; C_1 and C_2 are acceleration factors (usually 2); r_{1i} and r_{2i} are two values picked from 0 to 1 randomly.

PSO's stochastic nature limits its predictive accuracy in a single run. Therefore, multiple runs are performed, and statistical data are compared to evaluate the proposed approach's effectiveness. This study only presents the results from a single run.

3.6. Cross validation

The use of 2-fold cross-validation (CV) is a common strategy for addressing the issue of limited data sets that can lead to overfitting errors (Cawley Gavin and Talbot Nicola, 2010). Additionally, hyperparameters are modified on a randomly divided training set sample (external set) that consists of 70% of the original data. Furthermore, the external training data is split into a validation set (10%) and an internal training set (90%). PSO is used to find optimal BPNN hyperparameters on the internal training set. Moreover, the model's parameters are evaluated by computing the RMSE of the verification set. This process is repeated five times to obtain ten RMSE values. To configure the ANN model, the model hyperparameters with the RMSE that have the smallest values will be chosen. Fig. 6 illustrates the BPNN model training procedure using 2-fold CV and PSO.

$$RMSE = \sqrt{\frac{1}{N}\sum_{i=1}^{N}\left(y_i^{*} - y_i\right)^2} \tag{21}$$

$$R = \frac{\Sigma_{i=1}^{N}\left(y_i^{*} - \overline{y^{*}}\right)\left(y_i - \overline{y}\right)}{\sqrt{\Sigma_{i=1}^{N}\left(y_i^{*} - \overline{y^{*}}\right)^2}\sqrt{\Sigma_{i=1}^{N}\left(y_i - \overline{y}\right)^2}} \tag{22}$$

$$MAPE = \frac{1}{N}\sum_{i=1}^{n}\left|\frac{y_i^{*} - y_i}{y_i}\right| \tag{23}$$

$$MAE = \frac{1}{N}\sum_{i=1}^{n}\left|y_i^{*} - y_i\right| \tag{24}$$

where the root is the square error, N is the number of samples in the dataset, R is the correlation coefficient, y_i^{*} is the forecasted output of ML models, y_i is the real output in the dataset, $\overline{y^{*}}$ is the forecasted mean value, and $\overline{y}$ is the real mean value in the dataset, MAE is the absolute error, and $MAPE$ is the absolute percentage error used to assess the ML characteristics.

3.7. ML model visualization

The primary objective of employing machine learning is to generate decisions based on the model output. However, to achieve this goal, it is essential to ensure the interpretability of the machine learning model to understand its underlying processes and outputs. Considering machine learning is perceived as a "black box", the development of interpretable techniques for visualizing the model (both locally and globally) is highly valuable. One global interpretable technique is the Partial Dependence Plot (PDP), which enables the representation of the impact of one or two features on the model's output. Additionally, PDP can provide information on the nature of the relationship between the target and feature, whether it is linear, monotonic, or more complex. The technique was originally proposed by Friedman in 2001, where the partial dependency function of regression is expressed in Equation (25) (Friedman Jerome, 2001).

$$f_{xs}(x_s) = E_{xs}\left[f_{xs}(x_s, x_c)\right] = \int f_{xs}(x_s, x_c)dP(\ x_c) \tag{25}$$

where, x_s is the feature and the partial dependency function, f is the established ML model, and x_c is the other features in f. The feature (s) are selected features in the study. The feature vectors x_s and x_c define the whole feature space x. The link between the features in set C and the model output can be established by marginalizing the model output on the feature distribution in set C. A function that solely depends on the features in set S can be obtained by marginalizing other features.

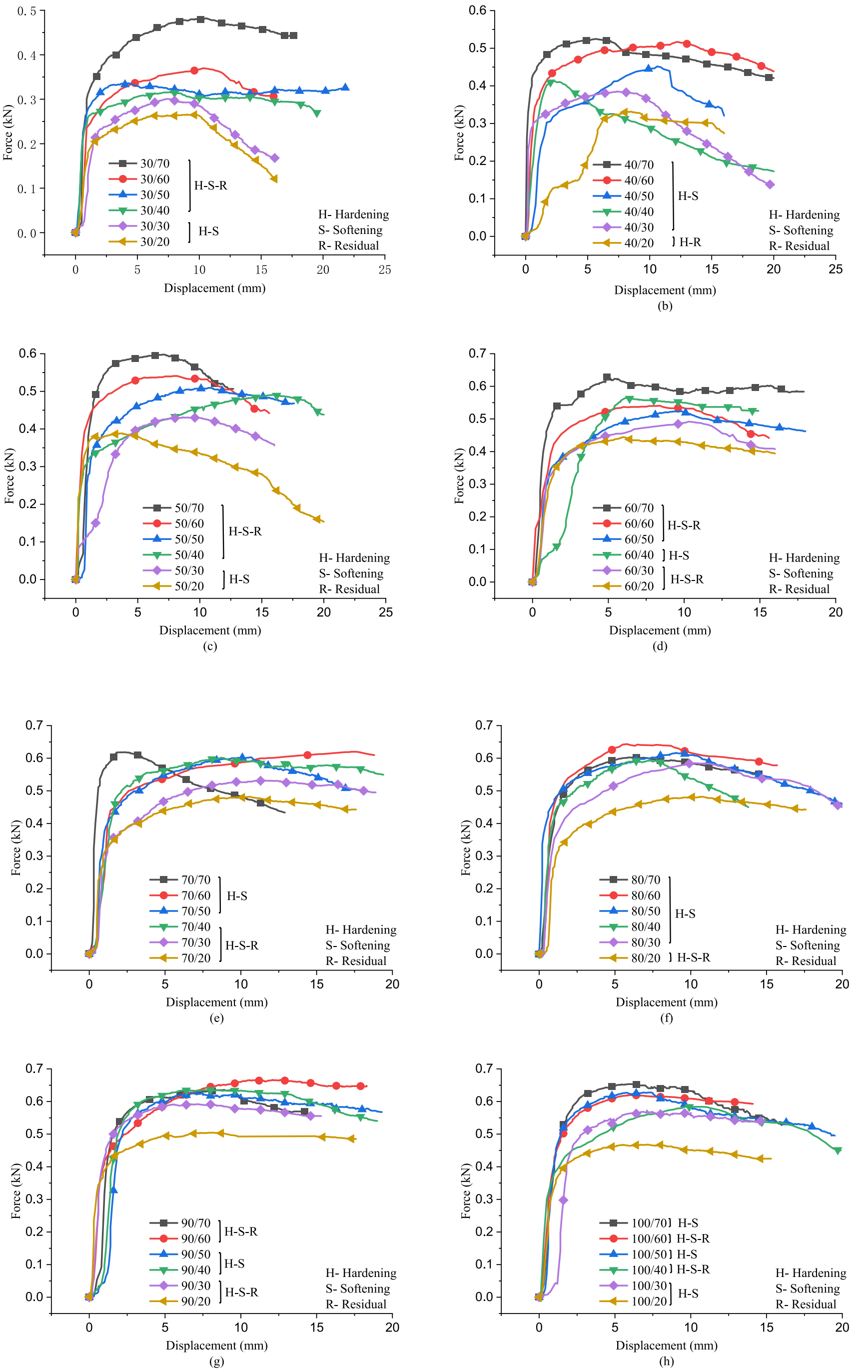

Fig. 7. The pullout force-displacement curves of anchor samples under different bond lengths: a) 30 mm; b) 40 mm; c) 50 mm; d) 60 mm; e) 70 mm; f) 80 mm; g) 90 mm; h) 100 mm.

4. Results and discussion

4.1. Experimental results for bond strength

A total of 48 pullout tests were conducted on anchor samples for this study. As outlined in Table 1, the samples were divided into eight groups based on their anchoring lengths, with each group containing six samples with different free/bond anchor length ratios. The resulting pullout force-displacement curve for each group is displayed in Fig. 7.

The force-displacement curve for each group shows that the free length of the anchor section significantly affects the pullout response when using relatively small bond lengths. For instance, as seen in Fig. 7 (a) and (b), when the free length is between 40 and 50 mm, the softening degree of the curves is not significant, and a residual zone appears in the range of pulling displacement. As the free length increases, the softening behavior becomes more apparent and turns into the residual section. Conversely, when the free length decreases, the softening phase also decreases, and a residual phase can be observed along the development of pullout displacement. Moreover, when the bond length is between 50 and 60 mm, the influence of the free length on the softening section of the curve decreases, showing similar trends for pullout response for each specimen. This trend remains when the bond length is increased to

Table 4
Ultimate average interface shear strength.

Bond length of the specimen (mm)	Free length of the specimen (mm)					
	20	30	40	50	60	70
	Ultimate average interface shear strength (kPa)					
30	134.58	103.31	93.88	88.33	84.04	74.27
40	109.94	108.27	94.66	86.49	80.62	69.53
50	100.18	90.63	85.35	82.26	72.21	65.05
60	87.88	75.53	73.21	78.74	68.69	62.13
70	74.04	74.19	72.16	72.04	63.66	57.68
80	63.14	67.40	64.60	62.22	61.25	50.47
90	59.21	62.04	58.64	59.19	55.11	47.00
100	55.14	51.93	52.60	48.92	48.00	39.20

70–80 mm, except for samples 70/70 and 80/40, which deviate from the overall trend with noticeable acceleration and softening. When the anchorage length increases to 90–100 mm, the abnormality disappears, and each curve shows good consistency. The influence of the free length on the pullout response is further reduced compared to other bond lengths.

The impact of free length on the pullout response (including the ultimate pullout strength and the softening behavior) can be explained by considering the load transfer process of the interface shear as follows: step a, the interface shear stress occurs along the bond length and propagate radially to the soils; step b, the soils surrounding the bond length get to shear subjected to the shear stress; step c, the soils surrounding the free length constrain the shear of the soils surrounding the bond length as overburden; step d, the soils surrounding the free length get compressed as their boundary is fixed by the upper plate (see Fig. 1).

Thus, the increasing free length corresponds to the increasing overburden of the soils surrounding the bond length, which results in the increasing pullout resistance (demonstrated as the peak pullout force). Meanwhile, the increasing free length corresponds to the increasing volume of the compressible soils, which leads to the increasing energy absorbing capacity (demonstrated as the post-peak softening degree of the pullout response curve).

Furthermore, the energy produced with pullout work is firstly absorbed by the sheared soils surrounding the bond length, and consecutively by the compressed soils surrounding the free length. Additionally, the specimens with small bond length will burden the main energy absorbing to the compressed soils surrounding the free length, which can manifest the different softening phase (see subfigs. 7a-c); whereas, the specimens with increased bond length will burden the main energy absorbing to the sheared soils surrounding the bond length, and the remaining energy absorbing for the compressed soils surrounding the free length is not sufficient to manifest the softening behavior (see subfigs. 7f-h).

Quantifying the pullout curve trend for different bond and free lengths combinations can be challenging. However, it is possible to establish a certain relationship through maximum pullout force analysis. Under the element test idea, the element anchor specimen used in this work is idealized as an element, which essentially corresponds to the uniform distribution of interface shear stress over the interface area. This idealization is connotated with the geotechnical element testing methods, such as direct shear test and triaxial compression test, where the uniformly distributed stresses over the loading area are used in the data processing of test results. Based on the above consideration, the maximum average interface shear strength was used by uniformly distributing the maximum pullout force monitored in the test over the interface area. Analyzing the effect of modifications in bond length on the average interface shear strength can reveal patterns. Table 4 and Fig. 8 illustrate such patterns.

Fig. 8 shows that changes in the free length configuration have an impact on the average ultimate interface shear strength, with an

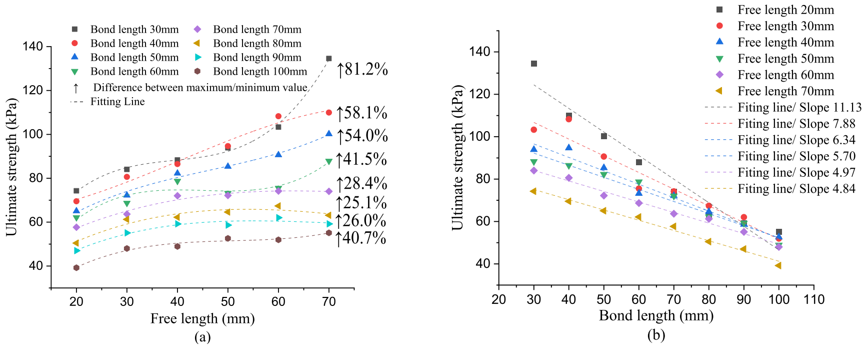

Fig. 8. Average ultimate interface shear strength against (a) free length; (b) bond length.

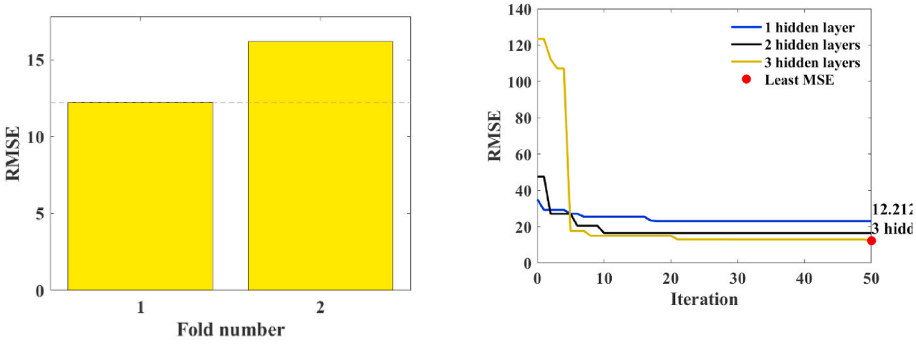

a) RSME values from 2 validation sets

b) RSME convergency

Fig. 9. Hyperparameters tuning for CS prediction.

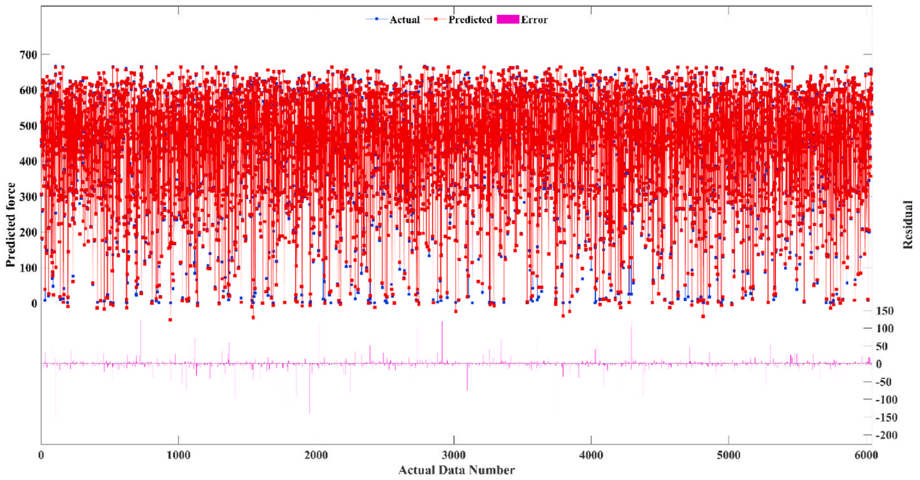

a) Training set

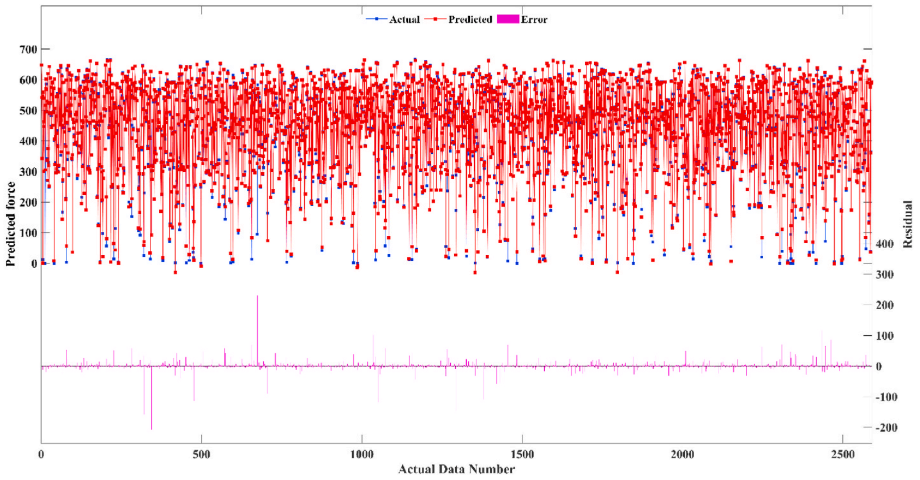

b) Test set

Fig. 10. Difference between predicted and actual bond strength.

increase in free length resulting in a higher average interface strength. The growth rate has no clear rules, and its rate depends on the bond length. For bond lengths between 30 and 80 mm, longer bond lengths result in smaller growth rates. However, for bond lengths greater than 80 mm, the growth rate increases with bond length. This means that specimens with a bond length of 80 mm have the smallest average interface strength increase when the free length of the section is changed.

Additionally, the average interface strength obtained from the pull-out test exhibits a clear linear decrease with an increase in bond length, as shown in Fig. 8(b). This means that the anchor's size effect in the unit interface test cannot be ignored. Regarding its linear decrease, the effect is insignificant when the free length of the section is less than 30 mm. Therefore, to reduce the sensitivity of the average interface strength, the combination of bond length and free length of the section should be between 20 and 80 mm.

4.2. *Modelling results for bond strength*

4.2.1. *Hyperparameter tuning*

The entire data set was split into two categories: the training set, which comprised 70% of the total data set and was employed for training in determining the most effective hyper-parameters, and the test set, which comprised 30% of the total data set and was utilized to assess the training algorithm's efficiency. As shown in Fig. 9(a), the BPNN containing the optimum hyperparameters is chosen from the first fold with the lowest RMSE. The corresponding RMSE convergency and PSO-adjusted hyperparameters are depicted in Fig. 9(b). The number of hidden layers and the neuros in each layer are hyperparameters of the BPNN which are tuned by utilizing PSO and 2-fold CV. It indicates that the RMSE reached its lowest level at the 23rd iteration of the first fold and remained constant throughout the remaining iterations (the number of hidden layers is 3). This indicates the successful convergence in the model training process. The final optimized framework of the BPNN is three hidden layers where the neuros' numbers are 46, 28, and 22, respectively. In addition, in the 70% training dataset, back propagation was utilized to revise the biased values as well as connection weights of BPNN using a uniform framework. The modified BPNN model was ultimately utilized to determine bond strength.

Fig. 10 depicts the comparison between forecasted and observed bond strength for testing and training datasets utilizing the optimal BPNN. Despite modest inaccuracies between the two sets, the PSO-BPNN model demonstrated accurate estimates for boned strength. As illustrated in Fig. 11, correlation coefficients were also used to evaluate the relationship between the forecasted and measured bond strength estimates. This model is reliable, as the training and test set coefficients were 0.9975 and 0.9948, respectively. Furthermore, the RMSE/R ratio was comparable for both sets, showing that the fitting was sufficient and

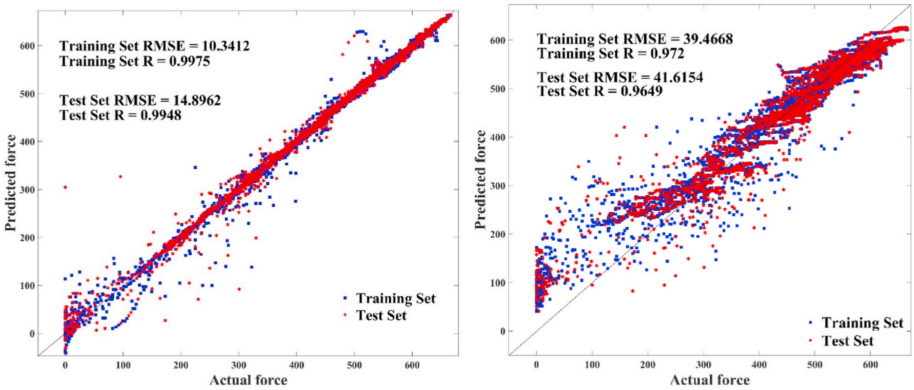

(a) PSO-BPNN

(b) PSO-RF

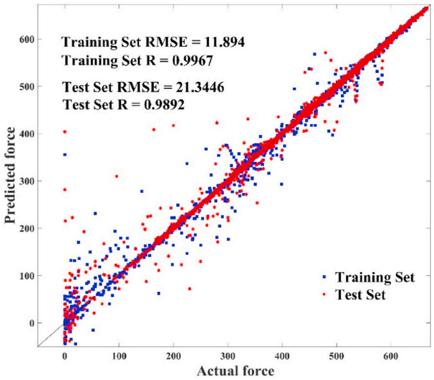

(c) PSO-SVR

Fig. 11. Predicted and actual bond strength for training and test sets.

without issues.

4.2.2. *Performance of PSO-BPNN*

This study compared the predictive capacity of the PSO-BPNN model with that of the RF and SVR models. Fig. 12(a) illustrates the variability between the predicted and actual bond strength results. The BPNN model showed the lowest median score (red line) and the narrowest interquartile range (blue square) compared to the other models. This indicates that the BPNN model had the lowest forecasting error among the three models. Even with multiple outliers, the BPNN model had the smallest upper limit (black line), demonstrating its superior accuracy in estimating bond strength. It is noted that the occurrence of these outliers could be attributed to several factors, including the limited diversity in our current dataset and potential limitations in the predictive capability of the applied ML algorithm, especially under extreme conditions or atypical data points.

Fig. 12(b) depicts the integration of three evaluation indices (RMSE, R, and standard deviation) using polar coordinates. The BPNN model had the highest accuracy as it was closest to the actual point on the Taylor diagram. It had the smallest RMSE, the highest R, and the smallest standard deviation compared to the other two models. Table 5 presents the operational statistics for the models investigated. The results show that the PSO-BPNN model is the optimal choice for forecasting bond strength.

The comparative analysis reveals that the PSO-BPNN model outperforms the RF and SVR models in predicting bond strength. This study suggests that the PSO-BPNN model can be an effective tool for forecasting bond strength in practical applications.

4.2.3. *Model visualization*

Partial Dependence Plot visualized the relationship between PSO-BPNN predicted force and selected features (free length, bond length, and displacement), as shown in Fig. 13. The x-axis and y-axis depict the features and the colour map exhibits the value distribution of the force which is calculated by the PSO-BPNN model. This extends the data space from the limited experimental samples to the unlimited samples within the feasible zone.

From subfigure 13a, the displacement with around 8 mm corresponds to the largest force, while the larger or lower displacement both correspond to lower force. Regarding to free length, it has slight influence on force when the displacement is lower than 2 mm, while it is positively related to force when the displacement is over 2 mm. This finding is consistent with the observations in the experiment. It can be seen in subfigure 13b that, similar to that of free length, the bond length has little impact on force on the condition of the low displacement. Moreover, the bond strength of 9 mm corresponds to the largest ultimate force. As illustrated in the above section, free length and bond length are two essential factors determining the anchoring interface characterization. Subfigure 13c compares the effect of the two factors on force and simultaneously provides the visualization. It can be observed that bond length is slightly more important than free length in terms of the effect on force.

In fact, the pullout forces variation over the bond length-free length-pullout displacement as shown in Fig. 13, is essentially an extensive and alternative illustration of pullout responses shown in Fig. 7. As above-mentioned in interpreting the pullout response, the work produced along with the development of the pullout force is companied with the load-transfer of interface shear and the energy absorbing of the soils surrounding the anchor. The varied combinations of bond\free length

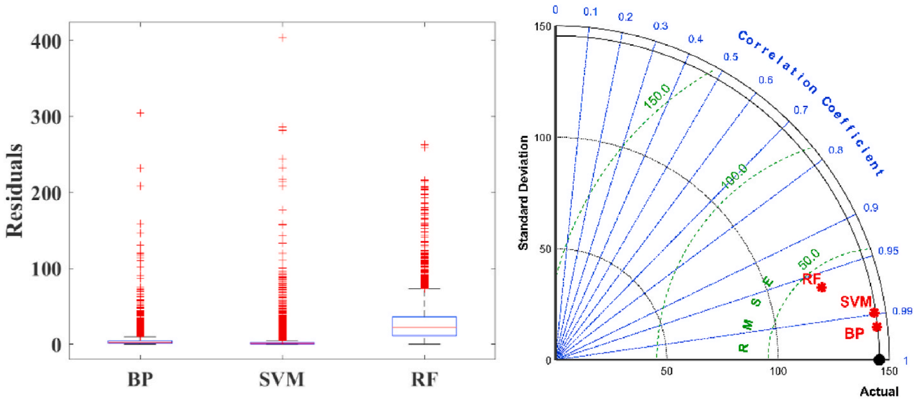

(a) Boxplot

(b) Taylor diagram

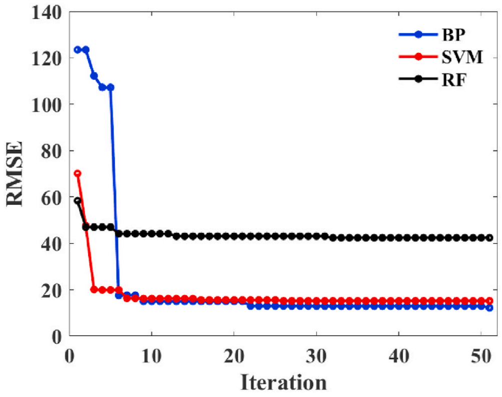

(c) Iteration diagram

Fig. 12. Performance evaluation of the three models for forecasting bond strength.

Table 5

Evaluation of ML models on the bond strength.

Evaluation index	Model		
	BPNN	SVR	RF
RMSE (kPa)	14.89620733	21.34460967	41.61542967
R	0.99750424	0.989202361	0.964864563
Time (s)	9019.054	342246.507	72.521

affect the energy absorbing proportions of the compressed soils surrounding the free length and the sheared soils surrounding the bond length. The development of pullout displacement essentially corresponds to the evolution of time along with the energy absorbing process, as the pullout force was applied using velocity-controlled loading. Since the work produced in the initial phase of pullout force is minor, and can be absorbed quickly by a small part of the sheared soils surrounding the bond length with no need to mobilize the extensive part of soils, the impact of the increasing bond length and free length on the pullout force is negligible with lower displacement (as observed in subfigures 13a and 13b).

5. Conclusions

The current research aimed to investigate the impact of free/bond length on the anchorage bond strength behavior. To this end, three ML models, namely PSO-BPNN, SVR, and RF, were developed using the experimental data to predict the bond strength. Among these models, the PSO-BPNN model provided the most accurate predictions that closely matched the measured experimental results. Based on the findings, the following conclusions were drawn from the study:

1. When specimens have the same bond length, variations in the free length section significantly impact the pullout response of the anchor. As the bond length of the section reaches 90–100 mm, the pullout curve trend under different free lengths exhibits better consistency.
2. The size effect of the anchor must be considered, as the average ultimate interface shear strength displays an evident linear decrease trend with an increase in bond length. For element anchor pullout tests to characterize the anchoring interface behavior, selecting bond lengths of approximately 80 mm and free lengths of 20 mm in the section is advisable.
3. The hyperparameters of BAS-BPNN, SVR, and RF models were successfully acquired using the BAS algorithm and 2-fold cross-validation. The BAS-BPNN model demonstrated a superior ability to forecast, with R values of 0.9975 and 0.9948 for bond strength and peak strain, respectively, outperforming the other models and demonstrating its higher accuracy.
4. PDP visualized the relationship between PSO-BPNN predicted force and three features (free length, bond length, and displacement). The displacement of around 8 mm and bond length of around 9 mm provide the highest bond force.

The presented experimental and data-driven modelling can provide insights into the application of element pullout test to the interface characterization of ground anchors, especially into the size configuration in preparing the element anchor specimens. Engineers can employ

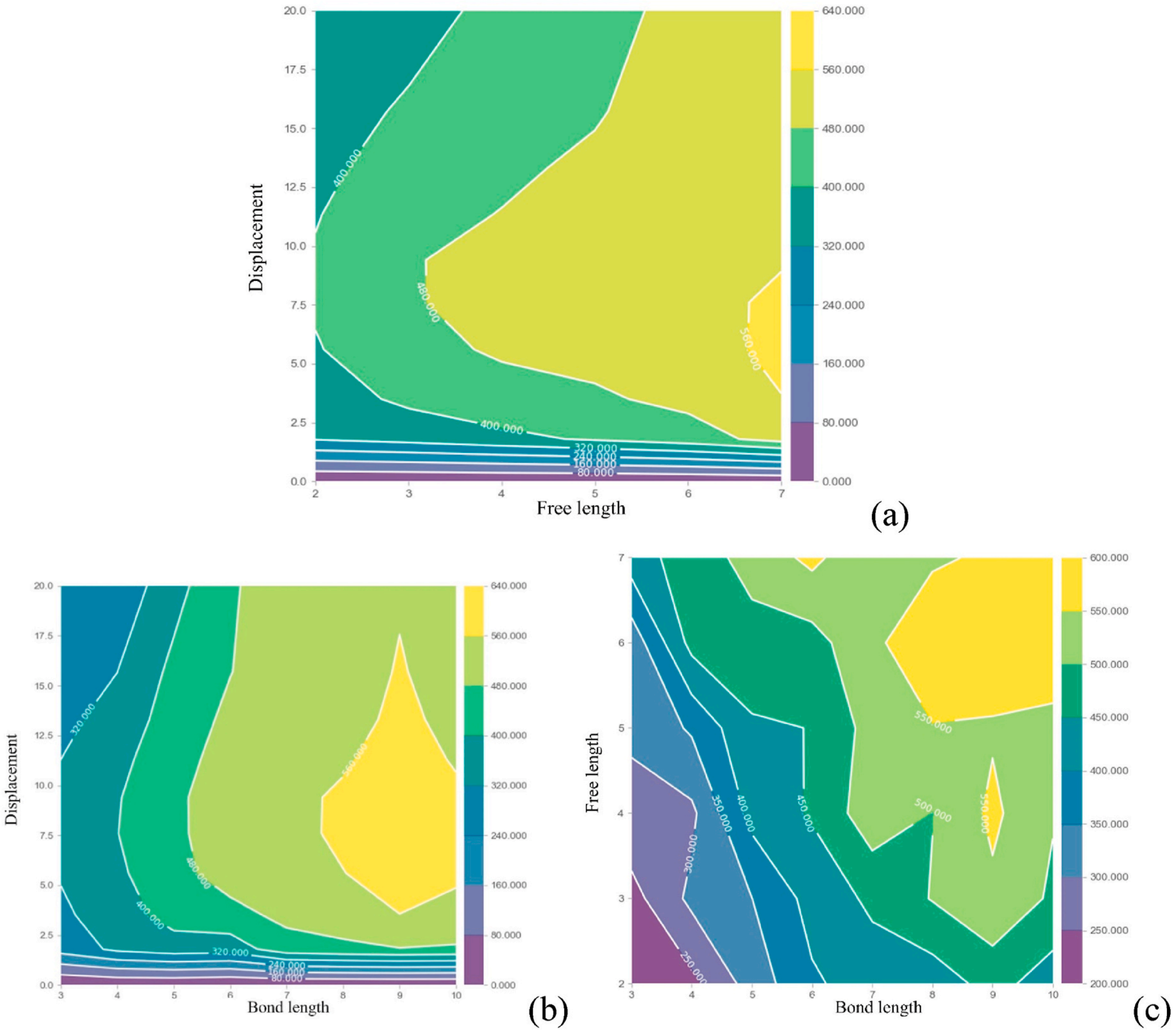

Fig. 13. Visualization of predicted force using PDP (a) force - free length - displacement (b) force -bond length - displacement (c) force - bond length - free length.

the presented data-driven model to estimate the interface strength of ground anchors in practice straightforward from the laboratory configurations of element anchor specimens. However, the presented modelling was completed in this work using specific soils and grouts, the extensive application of the modelling to anchors embedded in other types of soils is not recommended without further experimental validations. The models are recommended to be adjusted by enlarging the database if the difference of the cement (or tendon) between others and the used one is significant. In the future, more possible influencing factors need to be investigated such as the tendon type, soil components, etc.

CRediT authorship contribution statement

Genbao Zhang: Methodology, Conceptualization. **Changjie Xu:** Methodology, Formal analysis. **Yufei Wang:** Methodology, Formal analysis. **Junbo Sun:** Supervision, Conceptualization. **Haibin Ding:** Writing – original draft, Formal analysis. **Shimin Zhu:** Writing – original draft, Formal analysis. **Zefeng Zou:** Visualization, Validation. **Hisham Al azzani:** Writing – review & editing. **Zhiping Li:** Visualization, Validation. **Danqi Li:** Visualization, Validation. **Xiangyu Wang:** Supervision, Conceptualization.

Declaration of competing interest

The authors declare that they have no known competing financial interests or personal relationships that could have appeared to influence the work reported in this paper.

Data availability

Data will be made available on request.

Acknowledgements

This work was sponsored by National Key R&D Program of China (Grant number: 2023YFC3009400), Post-Doctoral Research Project of Jiangxi Province (Grant number: 2021KY59), National Natural Science Foundation of China (Grant numbers: 52238009, 51908201), and Key Project of Scientific Research of Hunan Education Department (Grant number: 21A0511). The authors appreciate their supports.

References

Abido, M.A., 2002. Optimal power flow using particle swarm optimization. Int. J. Electr. Power Energy Syst. 24 (7), 563–571. https://doi.org/10.1016/S0142-0615(01)00067-9.

Aiqing, She, Wang, Linjun, Peng, Yunlong, et al., 2023. Structural reliability analysis based on improved wolf pack algorithm AK-SS. In: Structures. Elsevier.

Bjarte, Grindheim, Li Charlie, C., et al., 2023. Full-scale Pullout Tests of Rock Anchors in a Limestone Quarry Focusing on Bond Failure at the Anchor-Grout and Grout-Rock Interfaces.

Boyd, Stephen, Lieven, Vandenberghe, 2004. Convex Optimization. Cambridge University Press, Cambridge.

Breiman, Leo, 1996. Bagging predictors. Mach. Learn. 24 (2), 123–140. https://doi.org/10.1007/BF00058655.

Burges, Christopher, 1998. A tutorial on support vector machines for pattern recognition. Data Min. Knowl. Discov. 2 (2), 121–167.

Cao, Jixing, Ser-Tong, Quek, Xiong, Haibei, et al., 2023a. Comparison of constrained unscented and cubature Kalman filters for nonlinear system parameter identification. J. Eng. Mech. 149 (11), 04023088 https://doi.org/10.1061/JENMDT.EMENG-7091.

Cao, Jixing, Bu, Fanfu, Wang, Jianze, et al., 2023b. Reconstruction of full-field dynamic responses for large-scale structures using optimal sensor placement. J. Sound Vib. 554, 117693. https://doi.org/10.1016/j.jsv.2023.117693.

Cawley Gavin, C., Talbot Nicola, L.C., 2010. On over-fitting in model selection and subsequent selection bias in performance evaluation. J. Mach. Learn. Res. 11, 2079–2107.

Chen, Changfu, Zhang, Genbao, Zornberg, Jorge G., et al., 2018. Interface behavior of tensioned bars embedded in cement-soil mixtures. Construct. Build. Mater. 186, 840–853. https://doi.org/10.1016/j.conbuildmat.2018.07.211.

Chen, Changfu, Zhang, Genbao, Jorge Gabriel, Zornberg, et al., 2019. Element Nail Pullout Tests for Prediction of Soil Nail Pullout Resistance in Expansive Clays. ASTM International.

Chen, C., Zhang, G., Zornberg, J.G., et al., 2020. Interface bond behavior of tensioned glass fiber-reinforced polymer (GFRP) tendons embedded in cemented soils. Construct. Build. Mater. 263, 120132 https://doi.org/10.1016/j.conbuildmat.2020.120132.

Chen, Changfu, Zhu, Shimin, Zhang, Genbao, et al., 2021. Time-dependent load transfer behavior of grouted anchors in laterite. Comput. Geotech. 132, 103969 https://doi.org/10.1016/j.compgeo.2020.103969.

Chen, C., Zhu, S., Zhang, G., et al., 2022a. Interface creep behavior of tensioned GFRP tendons embedded in cemented soils. Geosynth. Int. 29 (3), 241–253. https://doi.org/10.1680/jgein.21.00008.

Chen, Rui, Cheng, Zhou, Cheng, Li-Li, 2022b. Computer-vision-guided semi-autonomous concrete crack repair for infrastructure maintenance using a robotic arm. AI Civ. Eng. 1 (1), 9. https://doi.org/10.1007/s43503-022-00007-7.

Cheng, Y.M., Au, S.K., Yeung, Albert, 2016. Laboratory and field evaluation of several types of soil nails for different geological conditions. Can. Geotech. J. 53 (4), 634–645. https://doi.org/10.1139/cgj-2015-0267.

Cheng-Yu, Hong, Yi-Fan, Zhang, Guo, Jun-Wei, et al., 2016. Experimental study on the influence of drillhole roughness on the pullout resistance of model soil nails. Int. J. GeoMech. 16 (2), 04015047 https://doi.org/10.1061/(ASCE)GM.1943-5622.0000491.

Fernández-Martínez, Juan L., MuñIZ Zulima, Fernández, 2020. The curse of dimensionality in inverse problems. J. Comput. Appl. Math. 369, 112571 https://doi.org/10.1016/j.cam.2019.112571.

Fontana Casey, M., Hallowell Spencer, T., Arwade, Sanjay R., et al., 2019. Spatial coherence of ocean waves in multiline anchor systems for floating offshore wind turbines. Ocean Eng. 184, 59–73.

Friedman Jerome, H., 2001. Greedy function approximation: a gradient boosting machine. Ann. Stat. 1189–1232.

Hu, Wei, Lin, Zhi, Wang, Hui, et al., 2023. Method for calculating the uplift capacity of a circular anchor plate at arbitrary depth in sand. Ocean Eng. 286, 115441.

Huang, Hua, Yao, Yifan, Liang, Cunjun, et al., 2022. Experimental study on cyclic performance of steel-hollow core partially encased composite spliced frame beam. Soil Dynam. Earthq. Eng. 163, 107499 https://doi.org/10.1016/j.soildyn.2022.107499.

José Antonio, Schiavon, Hollanda Cavalcanti, Tsuha, et al., 2019. Monotonic, cyclic and post-cyclic performances of single-helix anchor in residual soil of sandstone, 11 (4), 824–836.

Lahiri, S.K., Chandra, Ghanta, 2008. The support vector regression with the parameter tuning assisted by a differential evolution technique: study of the critical velocity of a slurry flow in a pipeline. Chem. Ind. Chem. Eng. Q. 14 (3), 191–203.

Medvedeva, Marina A., Simos, Theodore., Charalampos, Tsitouras, 2020. Variable step-size implementation of sixth-order Numerov-type methods. Math. Methods Appl. Sci. 43 (3), 1204–1215. https://doi.org/10.1002/mma.5929.

Ren, F.F., Yang, Z.J., Chen, J.F., et al., 2010. An analytical analysis of the full-range behaviour of grouted rockbolts based on a tri-linear bond-slip model. Construct. Build. Mater. 24 (3), 361–370. https://doi.org/10.1016/j.conbuildmat.2009.08.021.

Ren, Chonghong, Yu, J.I.N., Liu, Xueying, et al., 2022. Cyclic constitutive equations of rock with coupled damage induced by compaction and cracking. Int. J. Min. Sci. Technol. 32 (5), 1153–1165. https://doi.org/10.1016/j.ijmst.2022.06.010.

Schapire, Robert E., 2003. The boosting approach to machine learning: an overview. In: Denison, D.D., et al. (Eds.), Nonlinear Estimation and Classification. Springer New York, New York, NY, pp. 149–171.

Shi, J., Lu, Y., Zhang, J., 2020. Approximation attacks on strong PUFs. IEEE Trans. Comput. Aided Des. Integrated Circ. Syst. 39 (10), 2138–2151. https://doi.org/10.1109/TCAD.2019.2962115.

Sun, Yuantian, Zhang, Junfei, Guichen, Li, et al., 2019a. Determination of Young's modulus of jet grouted coalcretes using an intelligent model. Eng. Geol. 252, 43–53.

Sun, Junbo, Zhang, Junfei, Gu, Yunfan, et al., 2019b. Prediction of permeability and unconfined compressive strength of pervious concrete using evolved support vector regression. Construct. Build. Mater. 207, 440–449. https://doi.org/10.1016/j.conbuildmat.2019.02.117.

Sun, Yuantian, Guichen, Li, Zhang, Junfei, et al., 2020. Development of an Ensemble intelligent model for assessing the strength of cemented paste backfill. Adv. Civ. Eng. 2020, 1643529 https://doi.org/10.1155/2020/1643529.

Sun, Junbo, Wang, Yufei, Liu, Shukui, et al., 2021a. Mechanical, chemical and hydrothermal activation for waste glass reinforced cement. Construct. Build. Mater. 301, 124361.

Sun, Junbo, Wang, Yufei, Yao, Xupei, et al., 2021b. Machine-learning-Aided prediction of flexural strength and ASR expansion for waste glass cementitious composite. Appl. Sci. 11 https://doi.org/10.3390/app11156686.

Sun, Junbo, Yongzhi, Ma, Jianxin, Li, et al., 2021c. Machine learning-aided design and prediction of cementitious composites containing graphite and slag powder. J. Build. Eng. 43, 102544 https://doi.org/10.1016/j.jobe.2021.102544.

Sun, Junbo, Wang, Xiangyu, Zhang, Junfei, et al., 2021d. Multi-objective optimisation of a graphite-slag conductive composite applying a BAS-SVR based model. J. Build. Eng. 44, 103223 https://doi.org/10.1016/j.jobe.2021.103223.

Sun, Junbo, Tang, Yunchao, Wang, Jianqun, et al., 2022a. A multi-objective optimisation approach for activity excitation of waste glass mortar. J. Mater. Res. Technol. 17, 2280–2304.

Sun, Yuantian, Bi, Ruiyang, Sun, Junbo, et al., 2022b. Stability of roadway along hard roof goaf by stress relief technique in deep mines: a theoretical, numerical and field study. Geomechanics and geophysics for geo-energy and geo-resources 8 (2), 45.

Sun, Junbo, Wang, Jiaqing, Zhu, Zhaoyue, et al., 2022c. Mechanical performance prediction for sustainable high-strength concrete using bio-inspired neural network. Buildings 12 (1), 65.

Vinay, Chandwani, Agrawal, Vinay, Ravindra, Nagar, 2015. Modeling slump of ready mix concrete using genetic algorithms assisted training of Artificial Neural Networks. Expert Syst. Appl. 42 (2), 885–893. https://doi.org/10.1016/j.eswa.2014.08.048.

Wang, Xiangyu, Jun, Wang, Wu, Chenke, et al., 2022. Engineering brain: metaverse for future engineering. AI Civ. Eng. 1 (1), 2.

Wanhui, Feng, Wang, Yufei, Sun, Junbo, et al., 2022. Prediction of thermo-mechanical properties of rubber-modified recycled aggregate concrete. Construct. Build. Mater. 318, 125970 https://doi.org/10.1016/j.conbuildmat.2021.125970.

Yan, Yang, Lin, Benqing, Zhang, Wei, 2023. Experimental and numerical investigation of an arch–beam joint for an arch bridge. Arch. Civ. Mech. Eng. 23 (2), 101. https://doi.org/10.1007/s43452-023-00645-3.

Yang, Su, Jun, Wang, Danqi, Li, et al., 2023. End-to-end deep learning model for underground utilities localization using GPR. Autom. ConStruct. 149, 104776 https://doi.org/10.1016/j.autcon.2023.104776.

Yao, Yifan, Zhou, Liqi, Huang, Hua, et al., 2023. Cyclic performance of novel composite beam-to-column connections with reduced beam section fuse elements. In: Structures. Elsevier.

Yuanbo, Xu, Wang, En, Yang, Yongjian, et al., 2021. A unified collaborative representation learning for neural-network based recommender systems. IEEE Trans. Knowl. Data Eng. 34 (11), 5126–5139. https://doi.org/10.1109/TKDE.2021.3054782.

Zhang, Genbao, Chen, Changfu, Zornberg, Jorge G., et al., 2020a. Interface creep behavior of grouted anchors in clayey soils: effect of soil moisture condition. Acta Geotech. 15, 2159–2177.

Zhang, Junfei, Sun, Yuantian, Guichen, Li, et al., 2020b. Machine-learning-assisted shear strength prediction of reinforced concrete beams with and without stirrups. Eng. Comput. 1–15.

Zhang, Genbao, Chen, Changfu, Kefei, Li, et al., 2022a. Multi-objective optimisation design for GFRP tendon reinforced cemented soil. Construct. Build. Mater. 320, 126297.

Zhang, Genbao, Chen, Changfu, Sun, Junbo, et al., 2022b. Mixture optimisation for cement-soil mixtures with embedded GFRP tendons. J. Mater. Res. Technol. 18, 611–628.

Zhang, Genbao, Chen, Changfu, Zhang, Yuhao, et al., 2022c. Optimised neural network prediction of interface bond strength for GFRP tendon reinforced cemented soil. Geomech. Eng. 28 (6), 599–611.

Zhang, Lei, Xiaobin, Li, Wang, Jiangchao, et al., 2023. Mechanical response of dropping a Hall anchor and its penetration depth in riverbed silt. Ocean Eng. 281, 114845.

Zhang, Chunwei, Duan, Cunkun, Sun, Li, 2024a. Inter-storey isolation versus base isolation using friction pendulum systems. Int. J. Struct. Stabil. Dynam. 24 (2), 2450022 https://doi.org/10.1142/S0219455424500226.

Zhang, Wei, Zhang, Shiqi, Jiangang, Wei, et al., 2024b. Flexural behavior of SFRC-NC composite beams: an experimental and numerical analytical study. In: Structures. Elsevier.

Zhu, Shimin, Chen, Changfu, Zhang, Genbao, et al., 2022. Theoretical and experimental investigations of anchoring force loss behavior for prestressed ground anchors. Can. Geotech. J. 59 (9), 1587–1601. https://doi.org/10.1139/cgj-2021-0220.

Zou, Jin-Feng, Zhang, Peng-Hao, 2019. Analytical model of fully grouted bolts in pull-out tests and in situ rock masses. Int. J. Rock Mech. Min. Sci. 113, 278–294. https://doi.org/10.1016/j.ijrmms.2018.11.015.